

Article

Satellite Imagery Recording the Process and Pattern of Winter Temperature Field in Yangtze Estuary Interrupted by a Cold Wave

Ruirui Chen ¹ , Xuezhong Jiang ^{2,3,*} and Jing Chen ¹

¹ State Key Laboratory of Estuarine and Coastal Research, East China Normal University, Shanghai 200241, China

² The School of the Urban and Regional Science, East China Normal University, Shanghai 200241, China

³ Institute for Global Innovation & Development, East Normal University, Shanghai 200241, China

* Correspondence: xzjiang@sklec.ecnu.edu.cn; Tel.: +86-138-1679-2992

Abstract: Sea surface temperature (SST) is a key marine ecological metric. An optimized split-window algorithm was used to invert the Yangtze Estuary's temperature field during a cold wave process. Additionally, MODIS SST inversion results were used to explore the effects of typical cold waves on the Yangtze Estuary's temperature field through the application of a temperature profile analysis method and a multiscale, multidirectional edge detection algorithm. According to the findings, (1) the cold wave altered the temperature field characteristics and the temperature front intensity, morphology, and spatial distribution pattern within the Yangtze Estuary for a short period. The strong temperature front displayed irregular edges and scattered patterns due to the combined effects of cold water masses produced by the cold wave and the tides and the warm water currents outside the mouth. (2) The cold wave caused significant short-term deviations in the Yangtze Estuary's SST. The cold water tongue stretched across the entire Yangtze Estuary, where the temperature dropped sharply with time, with the maximum cooling occurring outside the mouth, at 12.2 °C, and the minimum cooling occurring inside the mouth, at only 5.5 °C. (3) The spatially gradual warming of the Yangtze Estuary's SST from inside to outside the mouth became a low–lower–high pattern during cold waves. (4) The cold wave exhibited a greater influence on the strength, form, and distribution of the temperature front. Studying the effects of cold waves on the Yangtze Estuary's temperature field has significant theoretical and practical implications for understanding the changes in the winter temperature field, environmental protection, disaster mitigation, and prevention.

Keywords: cold wave; MODIS; sea surface temperature; split-window algorithm; Yangtze Estuary



Citation: Chen, R.; Jiang, X.; Chen, J. Satellite Imagery Recording the Process and Pattern of Winter Temperature Field in Yangtze Estuary Interrupted by a Cold Wave.

Atmosphere **2023**, *14*, 479. <https://doi.org/10.3390/atmos14030479>

Academic Editor: Alfredo Rocha

Received: 19 January 2023

Revised: 23 February 2023

Accepted: 24 February 2023

Published: 28 February 2023



Copyright: © 2023 by the authors. Licensee MDPI, Basel, Switzerland. This article is an open access article distributed under the terms and conditions of the Creative Commons Attribution (CC BY) license (<https://creativecommons.org/licenses/by/4.0/>).

1. Introduction

Sea surface temperature (SST) is one of the most important parameters affecting marine environments. It is determined by solar radiation, water vapor heat exchange, ocean current motion, and water mass mixing [1]. SST can be used to characterize the thermal and dynamic processes of the ocean and to provide a framework for studying ocean phenomena, such as ocean circulation, mesoscale eddies, ocean fronts, upwelling, and ocean mixing [2]. Additionally, this parameter has a strong impact on the transport of materials, the occurrence of red tides, and the management of fisheries resources [3]. SST exhibits a uniform steady state when there are no strong external factors [4]; however, in estuarine coastal waters with strong land–sea interactions, the situation becomes more complex. The drastic changes in water temperature in the Yangtze Estuary waters changed various hydrological characteristics and patterns of the original waters, affecting aquatic ecology, including the distribution of surface chlorophyll a concentration, mariculture, and marine organisms [5,6], as well as the spawning and reproduction of fish that depend on stable water temperature changes (e.g., Chinese sturgeon) [7]. In the Yangtze Estuary, the

SST field exhibits distinct seasonal characteristics, which are mainly controlled by intense solar radiation in summer and runoff cold sources in winter [8]. Under the influence of tides, a distinct temperature front often occurs in mixed salty and fresh waters outside the mouth [9]. Such spatiotemporal characteristics and variations in estuarine waters can be attributed to complex intrinsic dynamics [10]. The Yangtze Estuary's SST is also influenced by El Niño climate patterns for long periods [11]. Short-term changes are difficult to analyze quantitatively because they may be influenced by violent weather processes, such as typhoons and cold waves, which occur for short periods of time, but during these processes, the SST can change drastically. With the advent and development of remote sensing, historical temperature changes in the Yangtze Estuary can now be reproduced, enabling dynamic monitoring of the process.

Much work was conducted by domestic and international researchers in the inversion of seawater surface temperature using satellite remote sensing techniques. There are many algorithms for SST inversion using thermal infrared remote sensing data, which are broadly classified into single-channel algorithms [12–16] and split-window algorithms [17–21] according to the number of thermal infrared channels involved in the inversion. Specifically, the split-window algorithm based on the radiative transfer equation has high flexibility and is widely used for the inversion of sea surface temperature. The main idea of this method is based on the radiative transfer model, which is simplified by a large number of simulations to a function containing several easily solvable parameters. Qin et al. (2001) used two parameters, surface-specific emissivity and atmospheric transmittance, as variables. The Wan–Dozier algorithm [22] is a full-view split-window algorithm for MODIS data. Wan et al. established a look-up table for the coefficients of the split-window algorithm by analyzing the relationship between parameters such as incident observation angle, water vapor content, lower atmospheric temperature, surface temperature, and lower atmospheric temperature through accurate measurements, and used the look-up table method to invert the surface temperature. Many domestic scholars made many improvements based on the Qin algorithm, such as linear simplification of the Planck function [23], simulation of the split-window algorithm parameters for the thermal infrared channel characteristics of the MODIS sensor [24], estimation of the sensor viewing angle on the atmospheric transmittance and the effect of surface temperature inversion [25], and optimization of the split-window surface temperature inversion algorithm considering the sensor observation angle [26]. In order to improve the accuracy of the algorithm, some scholars began to construct models from the perspective of the principle of two-way reflection and the infrared emissivity of objects [27], invert the temperature according to the difference of remote sensing data seen from different angles [28], use the method of uncertainty inversion [29], optimize the parameters of the split window algorithm [30], and introduce statistical methods and neural networks into the analysis of remote sensing satellite monitoring [31]. These above algorithm optimizations greatly improved the accuracy of surface inversion and the computational speed. The estuary area of the Yangtze River is close to the land, and the estuary is subject to the dual action of land runoff and ocean currents, with strong mixing of water bodies and strong convection phenomena that make the water–gas concentration greater than that of the open sea, so there are fewer studies and no inversion algorithms with higher accuracy.

Numerous scholars studied the sea surface temperature of the Yangtze estuary, mainly focusing on the time series variability and its underlying mechanisms [4,32–35]. A small number of scholars also analyzed sea surface temperature anomalies when a particular climatic effect is intense. Chen et al. (2005) found that sea surface temperature changes in the Yangtze estuary are more significantly affected by El Niño. Zhang et al. (2017) noted the negative anomalous contribution of typhoons to the sea surface temperature in the East China Sea. Based on the FVCOM-SWAVE regional ocean coupling model, Wang et al. (2016) conducted a simulation to study the ocean thermal kinetic energy changes in the Hangzhou Bay area of the Yangtze estuary during the winter half of the year under the influence of the cold wave process, i.e., it mainly characterized the sea current energy and

temperature difference energy. Ghasemi et al. (2020) explored the effects of SST and ENSO on precipitation in Indian Ocean waters [36]. Ma et al. (2022) found a possible remote correlation between SSTA and El Niño/La Niña timing in the South Pacific [37]. Ferster et al. (2018) study the SST dataset and SOI and Antarctic oscillation (AAO) remote correlations and find that SOI is negatively correlated with SST and positively correlated with AAO, and SOI and SST are better correlated [38]. The impact of such drastic weather changes as cold waves on the sea surface temperature of the Yangtze estuary is less explored.

The aim of this study was to research the winter temperature field process and pattern in the Yangtze Estuary, which is interrupted by the North Jiangsu coastal current driven by a cold wave. Based on daily MODIS observations collected during typical cold waves, we established a local SST inversion algorithm and then applied a temperature profile analysis method and a mathematical morphology edge detection algorithm to analyze and explore the effects of a cold wave on the Yangtze Estuary's temperature field characteristics in detail, including changes in the intensity, morphology, and spatial distribution of temperature fronts, changes in the temperature field, changes in the spatial pattern of the temperature field, changes in the intensity and location of temperature fronts, etc. This research will be a valuable reference for understanding the properties and changes in the temperature field of the Yangtze Estuary in the winter season, as well as the characteristics of the estuarine ecosystem and disaster mitigation and protection.

2. Data and Methods

2.1. Study Area

The study area is the Yangtze Estuary, located on the coast of the East China Sea and the northwestern edge of the western Pacific Ocean, which shows a spatial pattern of three levels of branching and four mouths into the sea. The Yangtze River inlet runoff has obvious seasonal variations. The Yangtze Estuary is a medium intensity tidal estuary, with informal half-day shallow tides inside the estuary and regular half-day tides outside the estuary. The tide difference has obvious seasonal and interannual variations, and is also influenced by external currents such as the Taiwan Warm Current, the East China Sea Coastal Current, and the North Jiangsu Coastal Current, making the Yangtze Estuary a very complex and variable environment. Water temperature changes in the Yangtze Estuary are complex due to several factors, including runoff, solar radiation, flow systems, and tides. In terms of seasonal variation, the SST in the Yangtze Estuary reaches its lowest value in February in winter and its highest value in August in summer. In terms of interannual variability, there are significant oscillation cycles in the SST of the Yangtze Estuary.

2.2. Cold Weather and Satellite Data

According to the Shanghai Central Meteorological Station, a typical cold wave, occurs when the daily average temperature decreases by 6 °C over 24 h or by 8 °C over 48 h due to the presence of strong cold air and the daily minimum temperature declines by 5 °C due to the presence of cold air [39]. The following three typical cold wave processes were selected for this research: the first, which lasted from 5 January to 8 January 2015, with a cooling range of between 8 °C and 10 °C within 48 h, was accompanied by significant cooling, precipitation, and strong winds, generating gusts of 6~7 in the Yangtze Estuary waters. Second, a cold wave occurred from 15 January to 17 January 2021, with cold air from the north affecting the Yangtze Estuary from north to south, resulting in a regional minimum temperature decrease by approximately 8 °C within 48 h, with gusts of up to 7~8, accompanied by northerly gales of up to 7~8. The third cold wave occurred from 24 December to 28 December 2021. Influenced by cold dense air moving south, the minimum temperature dipped by more than 8 °C in 48 h, with northerly wind gusts of 6~8 in the Yangtze Estuary waters, producing rainy and snowy weather conditions and icing (<http://www.weather.com.cn/weather1d/101020700.shtml/>, accessed on 27 November 2022).

Satellite data were provided by Terra/Aqua-MODIS, a key element of NASA's Earth Observing System (EOS) program, carried on both the Terra and Aqua satellites. MODIS images contain 36 spectral channels, including visible, near-infrared, and infrared spectra with spatial resolutions of 250 m, 500 m, and 1000 m. With their moderate spatial, temporal, and spectral resolutions and channel settings, MODIS images are well-suited for SST inversion [40]. NASA's MODIS data sharing network (<https://ladsweb.modaps.eosdis.nasa.gov/search/order/4/MOD021KM--61/2023-02-12..2023-02-26/DB/118,34,125,28>, accessed on 27 November 2022) was used to obtain daily MO(Y)D021KM L1B data from the above three cold wave processes. NASA's geometric correction tool, the MODIS Swath Tool, along with the MODIS geolocation data product MO(Y)D03, were used for fine geometric correction, projection, and stitching. Clouds were identified using the MODIS cloud mask product (MO(Y)D35 L2) to ensure cloud-free data acquisition. Furthermore, radiometric calibration was used to derive the emissivity, reflectivity, and satellite zenith angle characteristics. Subsequently, the preprocessing results were used in the inversion algorithm to obtain an SST dataset for the Yangtze Estuary during typical cold waves.

2.3. In Situ SST Measurements

The surface water temperature was measured for 26 December 2011, 27–28 May 2012, 21 May 2013, 24 July 2013, 1 January 2014, and 1–10 January 2018, in the Yangtze Estuary waters using ship fixed-point measurements, and the distribution of stations is illustrated in Figure 1. This temperature was measured with an optical backscatter point sensor (OBS) with an accuracy of 0.05. Based on marine operational conditions and hydrographic measurements, the OBS measures a water body's temperature 1 m underwater, while remote sensing inversion measures the surface temperature; these are different measurements. Donlon et al. (2002) found that the average difference between these two measurements is 0.17 °C, so this value was deducted from the actual difference in the calculation [41].

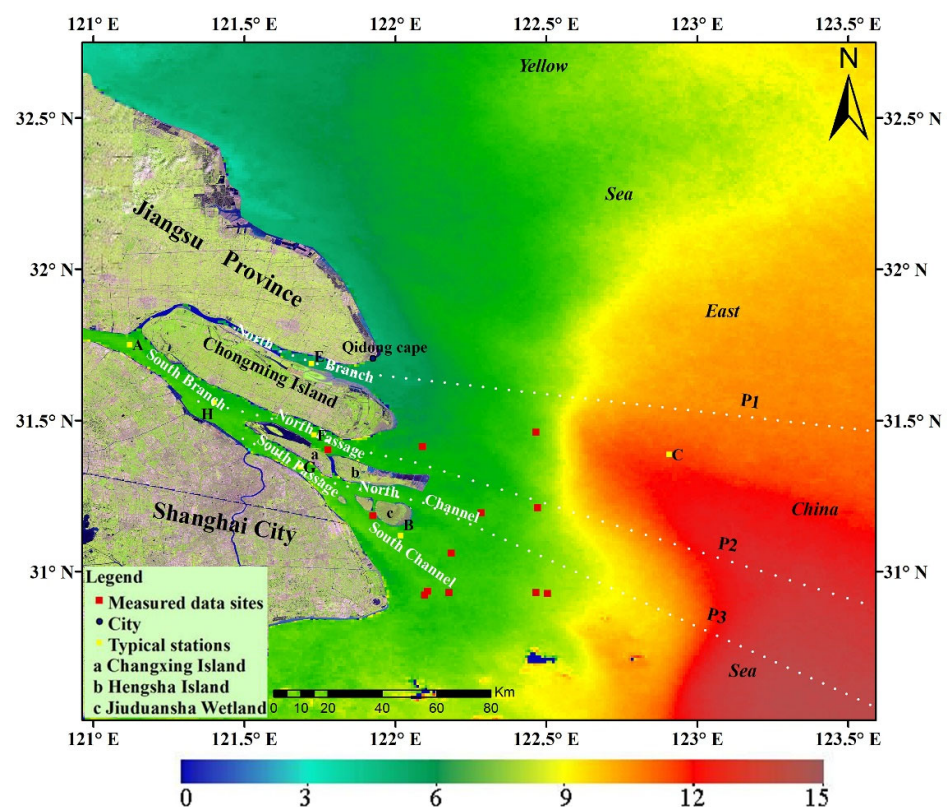


Figure 1. Multi-year mean SST in the Yangtze Estuary in January and sample sites, stations, and profiles (sites A (31.75° N, 121.12° E), B (31.06° N, 122.05° E), and C (31.38° N, 122.92° E), representing

inside the mouth, the mouth opening and outside the mouth of the Yangtze Estuary, respectively. E (31.69° N, 121.7° E), F (31.45° N, 121.73° E), G (31.35° N, 121.69° E), and H (31.55° N, 121.38° E) represent the North Branch, South Branch, North Passage, and South Passage, respectively. The SST at each reference location is represented by the average of the SST of 2 × 2 total of four pixels at that location. P1, P2, and P3 are the profiles of SST from inside the mouth to outside the mouth derived from a two-dimensional model using an orthogonal curve grid).

Additional SST data were collected from NASA’s Ocean Biology Processing Group (OBPG)’s SeaBASS (<https://seabass.gsfc.nasa.gov/search/sst>, accessed on 27 November 2022), which is a publicly accessible ocean and atmospheric real-world data platform. The platform includes data collected in situ within 30 min of satellite transit, with a product image within 10 km; the majority of these data are measurements collected by ships, NOAA’s in situ SST quality monitor Quam, and shipboard marine atmospheric emitted radiance interferometers (M-AERIs).

2.4. Construction of the SST Inversion Algorithm

This algorithm utilizes the different absorption properties of adjacent thermal infrared channels in the atmospheric window (11–13 m) to eliminate atmospheric influences and to obtain an inversion of the SST by linearly combining the brightness temperatures of the two channels [17]. In addition, using this algorithm, any interference produced by atmospheric thermal radiation on water vapor absorption can be decreased, and the problem of high atmospheric water vapor content in nearshore waters can be addressed. Furthermore, this algorithm can fully account for the parameters of bright temperature, atmospheric transmission, and specific emissivity, as well as various subsurface properties, with a simple and accurate model [23]. In this study, we present a high-precision algorithm based on Qin’s algorithm [42] that accounts for the characteristics of the water bodies in the Yangtze Estuary when calculating atmospheric transmittance, brightness temperature, and sea surface emissivity within the algorithm.

The algorithm was developed based on an equation representing the radiation transmitted from the ground to the infrared sensor. In the case where the surface and atmosphere are Lambertian bodies and the atmospheric downward radiation intensity in hemisphere space is constant, the equation can be reduced as follows [43]:

$$L_{\lambda} = \tau_{\lambda} \left(B_{\lambda}(T) \varepsilon_{\lambda} + (1 - \varepsilon_{\lambda}) L_{\lambda}^{\downarrow} \right) + L_{\lambda}^{\uparrow} \tag{1}$$

where L_{λ} is the brightness of the thermal radiation received by the sensor at wavelength λ , B_{λ} is the brightness of the thermal radiation emitted at wavelength λ by a blackbody with temperature T , T is the surface temperature, ε_{λ} is the specific emissivity of the surface at wavelength λ ($1 - \varepsilon_{\lambda}$ is the surface reflectance according to Kirchhoff’s law), τ_{λ} is the atmospheric transmittance from the ground to the remote sensor, and L_{λ}^{\uparrow} and L_{λ}^{\downarrow} are the atmospheric upward and downward thermal radiances, respectively. For a certain sensor band, the equation is given as follows [44]:

$$B_i(T_i) = \tau_i(\theta) \left(\varepsilon_i B_i(T_s) + (1 - \varepsilon_i) I_i^{\downarrow} \right) + I_i^{\uparrow} \tag{2}$$

where $B_i(T_i)$ represents the sensor’s received irradiance, T_i represents the brightness temperature in band i , T_s represents the surface temperature, and $\tau_i(\theta)$ represents the atmospheric transmittance at the sensor zenith angle θ . The following approximate derivations are given for I_i^{\uparrow} and I_i^{\downarrow} .

$$I_i^{\uparrow} = (1 - \tau_i(\theta)) B_i(T_a^{\uparrow}) \tag{3}$$

$$I_i^{\downarrow} = (1 - \tau_i(\theta)) B_i(T_a^{\downarrow}) \tag{4}$$

where T_a^\uparrow and T_a^\downarrow are the average atmospheric upward and downward temperatures, respectively, and Qin (2001) analytically showed that their equality does not affect the results. The equation is simplified as follows:

$$B_i(T_i) = \varepsilon_i \tau_i(\theta) B_i(T_s) + (1 - \tau_i(\theta))(1 + (1 - \varepsilon_i) \tau_i(\theta)) B_i(T_a). \tag{5}$$

The following equation is obtained by applying the linearly simplified Planck equation to the thermal infrared band of MODIS (B31, B32).

$$C_i = \varepsilon_i \tau_i(\theta); D_i = (1 - \tau_i(\theta))(1 + (1 - \varepsilon_i) \tau_i(\theta)) \tag{6}$$

$$B_{31}(T_{31}) = C_{31} B_{31}(T_s) + D_{31} B_{31}(T_a) \tag{7}$$

$$B_{32}(T_{32}) = C_{32} B_{32}(T_s) + D_{32} B_{32}(T_a) \tag{8}$$

where ε_i is the sea surface-specific radiance and $\tau_i(\theta)$ is the atmospheric transmittance at viewpoint θ . $B_i(T_j)$ at T is given via a Taylor expansion and simplification.

$$B_i(T_j) \approx B_i(T) + (T_j - T) \frac{\partial B_i(T)}{\partial T} = \frac{\partial B_i(T)}{\partial T} (P_i(T) + T_j - T) \tag{9}$$

$$P_i(T) = B_i(T) / \left(\frac{\partial B_i(T)}{\partial T} \right) \tag{10}$$

$$P_{31} = C_{31}(P_{31} + T_s - T_{31}) + D_{31}(P_{31} + T_a - T_{31}) \tag{11}$$

$$P_{32} + T_{32} - T_{31} = C_{32}(P_{32} + T_s - T_{31}) + D_{32}(P_{32} + T_a - T_{31}) \tag{12}$$

Fitting a $P_{31}(T_{31})$ and $P_{32}(T_{32})$ function across a given range of brightness temperatures, we obtain:

$$P_{31} = a_{31} T_{31} + b_{31} \text{ (average percentage residual 0.15\%)} \tag{13}$$

$$P_{32} = a_{32} T_{32} + b_{32} \text{ (average percentage residual 0.14\%)} \tag{14}$$

where $a_{31} = 0.438$, $b_{31} = -63.253$, $a_{32} = 0.471$, $b_{32} = -67.341$.

Eliminating T_a leaves only T_s and T_a in the original equation:

$$T_s = T_{31} + \frac{1}{E_0} (A_0 + A_1 T_{31} - A_2 T_{32}) \tag{15}$$

where each parameter is calculated as follows:

$$A_0 = b_{31} E_1 - b_{32} E_2 \tag{16}$$

$$A_1 = D_{31} + a_{31} E_1 \tag{17}$$

$$A_2 = D_{31} + a_{32} E_2 \tag{18}$$

$$E_0 = D_{32} C_{31} - D_{31} C_{32} \tag{19}$$

$$E_1 = D_{32}(1 - C_{31} - D_{31}) \tag{20}$$

$$E_2 = D_{31}(1 - C_{32} - D_{32}). \tag{21}$$

The brightness temperature, sea surface emissivity, and atmospheric transmittance are three critical Qin algorithm parameters for SST inversion, and the algorithm presented in this study considers the particular characteristics of the Yangtze Estuary in determining the three parameters.

2.5. Determination of Several Important Parameters

2.5.1. Brightness Temperature

Planck’s law provides a relationship between the brightness of a blackbody and its temperature, from which it is possible to derive the brightness temperature at a certain wavelength [23]:

$$L_B(T, \lambda) = \frac{hc^2}{\lambda^5 \left(e^{\frac{hc}{kT\lambda}} - 1 \right)} \tag{22}$$

where L_B is the blackbody irradiance brightness ($W \cdot m^{-2} \cdot sr^{-1} \cdot \mu m^{-1}$), $h = 6.626 \times 10^{-34}$ J·s, Planck’s constant; $k = 1.38 \times 10^{-23}$ J/K, Boltzmann’s constant; $c = 2.998 \times 10^8$ m/s, the speed of light; λ is the wavelength (m); and T is the blackbody thermodynamic temperature (K). By simplifying this equation, we obtain the following expression:

$$T = \frac{hc}{k\lambda \ln\left(\frac{hc^2}{\lambda^5 L_B} + 1\right)} = \frac{C_1}{\lambda \ln\left(\frac{C_2}{\lambda^5 L_B} + 1\right)} \tag{23}$$

where $C_1 = hc/k = 1.439 \times 10^{-2}$ K·m and $C_2 = hc^2 = 5.955 \times 10^{-17}$ K·m.

The spectral response function in a particular band range should be the integral of the product of the spectral radiance of the remote sensor detector and the spectral response function for that band since the sensor band has a bandwidth and the spectrum does not always perfectly respond to it [43,45].

$$L_b(T) = \frac{\int_{\lambda_{min}}^{\lambda_{max}} L(\lambda, T) f(\lambda) d\lambda}{\int_{\lambda_{min}}^{\lambda_{max}} f(\lambda, T) d\lambda} \tag{24}$$

A linear relationship between effective wavelength irradiance and spectral irradiance was established; the average difference between the fitted and actual values of the linear regression of the effective wavelength irradiance in the B31 band was approximately 0.0005 K·m, and the maximum difference was approximately 0.001 K·m, with excellent results. Consequently, the brightness temperature was more precise.

2.5.2. Sea Surface Emissivity

The sea surface emissivity is a function of wind speed and sensor zenith angle in the established inverse SST algorithms, based on the rough fitting results of Nicolas [46]. When the sensor angle of the view is greater than 45° [47], the sea surface emissivity is affected in a certain way, and the maximum observation angle of the MODIS sensor in the Yangtze Estuary can approach 65°. In the SST inversion, the fact that sea surface emissivity is affected by the wind speed and sensor angle of view must be considered.

$$\varepsilon_i(\theta, U) = \varepsilon_i(0^\circ) \left(\cos(\theta^{cU+d}) \right)^{b_i} \tag{25}$$

where $\varepsilon(\theta, U)$ is the sea surface emissivity and $\varepsilon(0^\circ)$ is the sea surface emissivity at an angle of view of 0°. For MODIS data, $\varepsilon_{31}(0^\circ) = 0.99229$, $\varepsilon_{32}(0^\circ) = 0.98823$, $c = -0.037 \pm 0.003$ s/m, $d = 2.360 \pm 0.003$, $b_{31} = 0.0342$, and $b_{32} = 0.0506$.

2.5.3. Atmospheric Transmittance

The atmospheric water vapor concentration can often be used to estimate atmospheric transmittance, and the inversion can be derived using Kaufman et al. (1992) [48]. The atmospheric water vapor content was estimated based on the ratio of the atmospheric window channel (B2) to the atmospheric absorption band (B19) of MODIS.

$$\frac{R_{19}}{R_2} = e^{\alpha - \beta\sqrt{W}} \tag{26}$$

where R_{19}/R_2 denotes the reflectance ratio of band 19 to band 2. $\alpha = 0.02$, and $\beta = 0.651$.

MODTRAN 4.0 was used to model the relationship between atmospheric transmittance and water vapor content after the atmospheric water vapor concentration was obtained. Furthermore, the environmental parameters used in the simulation were determined based on the climatic features and the location of the Yangtze estuary [49]. The atmospheric water vapor concentration and observed zenith angle were modified to model atmospheric transmittance at the effective wavelengths of the MODIS 31 and 32 bands for different situations. An essentially linear relationship between the water vapor content and atmospheric transmittance was established (Table 1).

Table 1. Relationship between atmospheric transmittance and water vapor content.

Water Vapor Content w (g/m^2)	Atmospheric Transmittance τ	R^2
Winter 0.0~1.4	$\tau_{31} = 0.9295 - 0.0939w$ $\tau_{32} = 0.9413 - 0.1009w$	0.9943 0.9904

The view angle [50] must be adjusted, and the atmospheric profile temperature must be corrected [22]. Atmospheric transmittance is influenced by both the view angle and the atmospheric temperature. In the absence of a precise analytical formula, linear simulations were carried out utilizing a look-up table or segmented functions, as shown in Table 2.

$$\Delta\tau_{31}(\theta) = -0.00247 + (2.3652 \times 10^{-5})\theta^2 \tag{27}$$

$$\Delta\tau_{32}(\theta) = -0.00322 + (3.0967 \times 10^{-5})\theta^2 \tag{28}$$

Table 2. Temperature correction function for atmospheric transmittance.

MODIS Band	Temperature Correction Function	Temperature Interval
B31	$\Delta\tau_{31}(T) = 0.08$	$T_{31} > 318$ K
	$\Delta\tau_{31}(T) = -0.05 + 0.00325(T_{31} - 278)$	$278 < T_{31} < 318$
	$\Delta\tau_{31}(T) = -0.05$	$T_{31} < 278$ K
B32	$\Delta\tau_{32}(T) = 0.095$	$T_{32} > 318$ K
	$\Delta\tau_{32}(T) = -0.065 + 0.004(T_{32} - 278)$	$278 < T_{32} < 318$
	$\Delta\tau_{32}(T) = -0.065$	$T_{32} < 278$ K

2.6. Accuracy Assessment

Indicating the algorithm’s precision by comparing the distance between measured and inverted values within 10 km and the difference in time within one hour is a more accurate method [51]. A total of 66 field measurements were chosen and synchronized with satellite observations and SST data from the SeaBASS database to evaluate the algorithm’s accuracy.

The root mean square error (RMSE) and mean absolute percentage error (MAPE) were used to evaluate the accuracy of the SST inversion algorithm and NASA’s standard SST product MOD28. A quantitative evaluation of the performance and precision of the models was conducted using the following equations:

$$RMSE = \sqrt{\frac{\sum_{i=1}^N (X_{situ,i} - X_{pre,i})^2}{N}} \tag{29}$$

$$MAPE = \frac{1}{N} \times \sum_{i=1}^N \frac{|X_{situ,i} - X_{pre,i}|}{X_{situ,i}} \times 100\% \tag{30}$$

where $X_{situ,i}$ is the field-measured SST, $X_{pre,i}$ is the modeled SST, and N is the total number of reference points.

The RMSE value of the SST algorithm inversion result was 0.58, and the MAPE value was 7.25%, while the validation results of the SST product MOD28 with measured data were 1.36 and 10.23%, respectively (Figure 2). This study’s SST inversion algorithm was more accurate than MOD28, making it better suited for local estuaries.

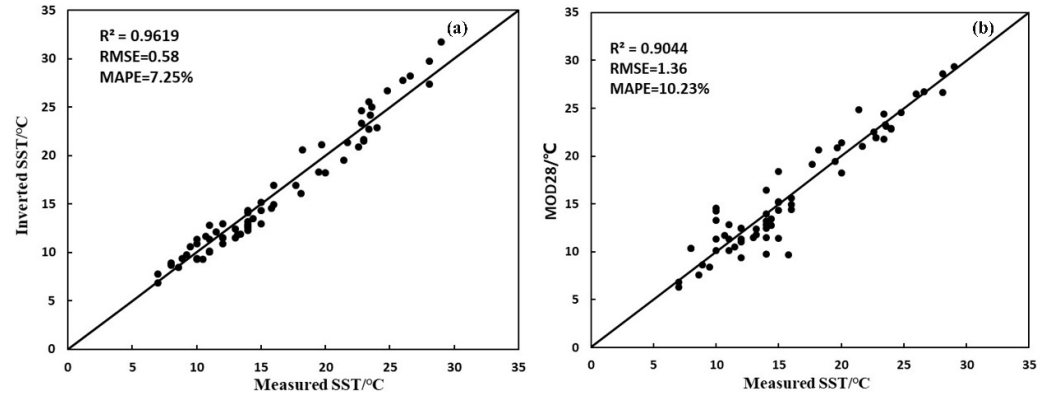


Figure 2. Calibration and validation of SST inversion algorithm and MOD28 to estimate sea surface temperature. Where, (a) is the validation of the remote sensing inversion results with the measured data; (b) is the validation of the SST product MOD28 with the measured data.

2.7. Edge Detection Algorithm Based on Mathematical Morphology

Taking the SST of the cold wave process as a reference value, a mathematical algorithm based on morphology was used to determine the boundary between water masses of different temperatures in the Yangtze Estuary. A key aspect of this algorithm was determining the appropriate structural elements and the edge operator.

A limited geographical extent and a limited scale of temperature fronts are associated with the Yangtze Estuary. To better identify the temperature front and filter out interference noise, multidirectional and suitable scale structural components were constructed using four structural elements with horizontal, vertical, 45° oblique, and 135° oblique orientations [52].

A modified edge detection operator based on the noise-resistant expansion-type operator and corrosion-resistant operator [49,53] was utilized in conjunction with the determined structural elements to acquire the boundary between water masses of different temperatures (i.e., temperature fronts) in the target image. The equations used are given as follows:

$$NEMO_{1m}(x,y) = [(f \circ s) \oplus s](x,y) - [(f \circ s) \cdot s](x,y) \tag{31}$$

$$NEMO_{2m}(x,y) = [(f \cdot s) \circ s](x,y) - [(f \cdot s) \odot s](x,y) \tag{32}$$

$$ED_i(x,y) = NEMO_{1m}(x,y) + E_{max}(x,y) - E_{min}(x,y) \tag{33}$$

$$E_{min}(x,y) = \min\{NEMO_{1m}(x,y), NEMO_{2m}(x,y)\} \tag{34}$$

$$E_{max}(x,y) = \max\{NEMO_{1m}(x,y), NEMO_{2m}(x,y)\}. \tag{35}$$

The edge detection findings $F(x,y)$, i.e., the temperature fronts, were obtained by using the foregoing equations along with the adaptive weighting method to calculate the edges detected by eight different structural components.

$$F(x,y) = \sum_{i=1}^8 W_i ED_i(x,y) \tag{36}$$

where W_i is the weight associated with edge ED_i computed using a single scale structure element.

A temperature gradient value GM of each frontal point image element, i.e., the frontal intensity, can be determined following the determination of the frontal point locations.

$$GM_{x,y} = \sqrt{\left(\frac{\partial SST}{\partial x}\right)^2 + \left(\frac{\partial SST}{\partial y}\right)^2} \quad (37)$$

$$GM_{m,n} = \sqrt{\left(\frac{\partial SST}{\partial m}\right)^2 + \left(\frac{\partial SST}{\partial n}\right)^2} \quad (38)$$

$$GM = \text{Max}GM_{x,y}, GM_{m,n} \quad (39)$$

$GM_{x,y}$ and $GM_{m,n}$ are the temperature gradient values in various directions, where x and y are taken as the east and north directions, respectively, while m and n are taken as the east–northwest 45° and north–northwest 45° directions.

An edge detection approach based on mathematical morphology may be of value in extracting the temperature fronts from the Yangtze Estuary, helping to preserve the information about the temperature fronts and to reflect their morphology and spatial distribution.

3. Results and Discussion

3.1. Characteristics of the Yangtze Estuary's Temperature Field without Effects from Cold Waves

The Yangtze Estuary's SST exhibits a spatial gradient (Figure 1), with temperatures increasing continuously from inside the mouth to outside the mouth as a result of the January inversion. Although the temperature is less than 4 °C inside the mouth and close to the shore, the water east of 123°E beyond the mouth of the southern trough reaches temperatures that exceed 15 °C. Consequently, there is a large temperature difference in the Yangtze Estuary, leading to a low–high temperature geographical distribution. The temperature change from inside the mouth to the mouth opening is usually modest, while the change from the mouth opening to outside the mouth is more extreme. The mainland is a source of cold water and the Yangtze River runoff carries that cold water downstream, which causes the SST inside the mouth and in the nearshore areas to be lower. A tongue-shaped warm water mass pointing southeast to the Yangtze Estuary is observed in the waters outside the mouth, which is influenced by the Northward Branch of the warm Taiwan current (ref). This results in a higher SST in the surrounding waters. There are large temperature gradients and dramatic changes in SST on both sides of the cold and warm water masses formed by runoff downstream near 122°30' E.

3.2. Characteristics of the Yangtze Estuary's Temperature Field before the Arrival of a Cold Wave

The northwest corner of the Yangtze Estuary along the coast of Qidong Cape is occupied by cold water before the occurrence of a cold wave, with an SST of less than 3 °C. Cold water masses extend to the southeast in the form of a tongue, the end of which reaches outside the North Passage. The tongue interacts with the nearshore flow system at the Yangtze Estuary, forming an east–west temperature front outside the North Branch and east of Chongming Island Beach. Furthermore, a tongue-shaped mass of warm water at 9~10 °C exists outside the mouth, which heads southeast toward the Yangtze Estuary, forming a broken bridge with the end of the cold water masses. This abrupt change in SST is accompanied by a prominent front near 122°30' E (Figure 3) and a temperature gradient of 0.9~1.8 °C/km. The front bulges to the west to 122°25' E and to the north to 31°30'32" N (Figure 4a,f). There is an average temperature gradient of 0.1 °C/km from inside the mouth to the mouth gate and 0.29 °C/km from the mouth gate to outside the mouth, with a distinct low-to-high spatial pattern (Figure 5). According to Figure 3, the changes in the temperature frontal interface patterns can be attributed to the interaction between runoff and tides in the estuary, as well as variations in tidal cycles. The outermost edge of the cold water mass and the tongue-shaped warm water have a more regular shape at low tide when the tidal force is relatively weak and Yangtze River runoff is relatively strong; the frontal interface is visible, and the edge of the front is regular (Figure 3a,b). At

high tide, the tidal force increases, the quantity and strength of the outward heat transfer from the warm water outside the mouth grow, and the temperature front tangent boundary grows, which is not immediately apparent (Figure 3c,d).

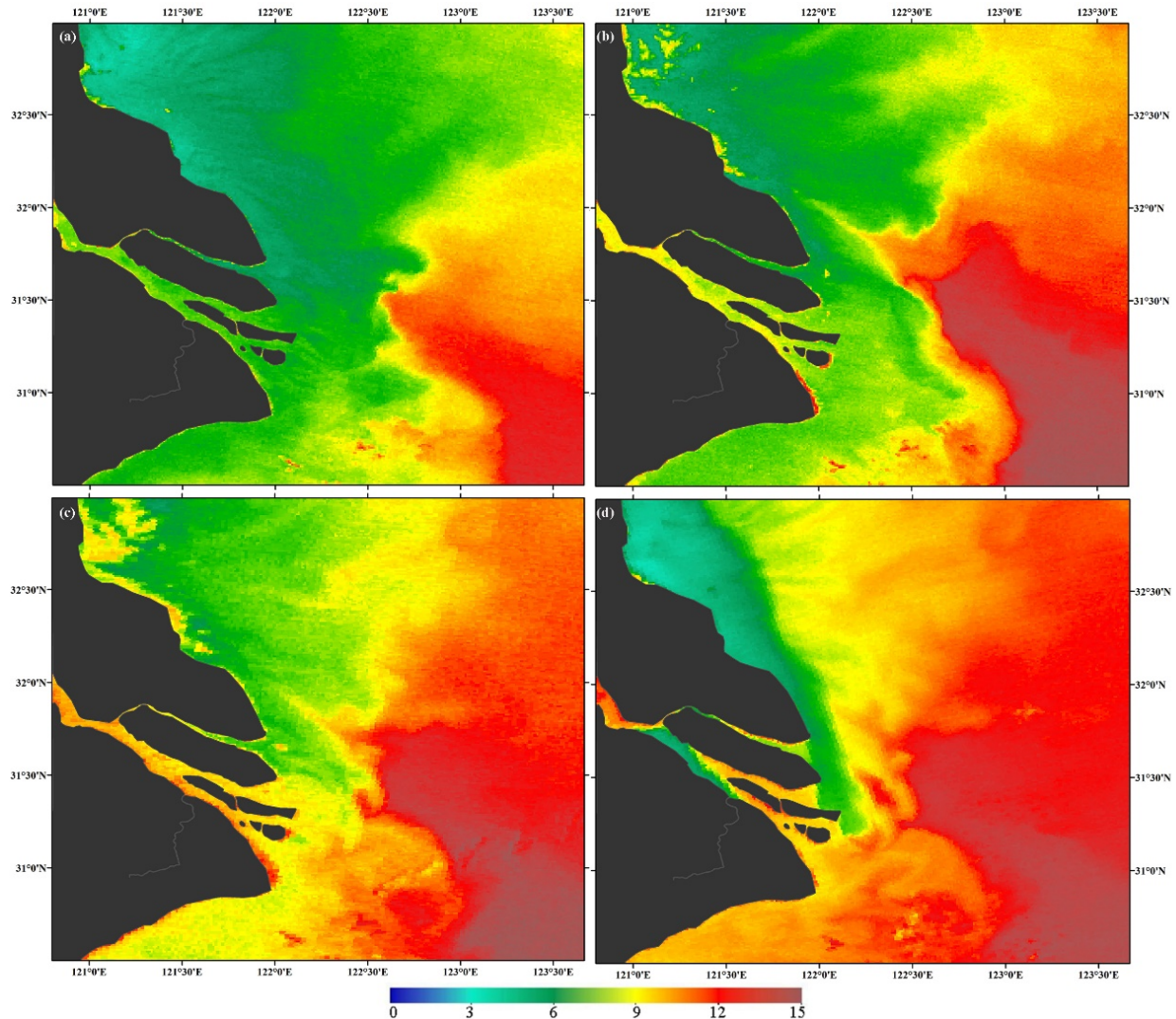


Figure 3. Characteristics of the SST field in the Yangtze Estuary before the cold wave (where (a–d) is 4 January 2015 (one day before the cold wave), 29 December 2014 (two days before the cold wave), 23 December 2021 (one day before the cold wave), and 22 December 2021 (two days before the cold wave), respectively).

3.3. Characteristics of the Yangtze Estuary's Temperature Field during a Cold Wave

A substantial amount of cold water is transported southward as a result of the combined wind and wind waves produced by a cold wave. A cold water mass crosses the whole Yangtze Estuary due to the enhanced power transmission of sea surface wind, wind, waves, and currents. Consequently, the Yangtze Estuary's SST decreases substantially and rapidly over the short term, and the temperature decreases steeply over time as a consequence of this phenomenon. There is a significant decrease outside the mouth, with a maximum temperature of 12.2 °C and an average temperature of 11 °C, followed by a decrease at the mouth opening, with a maximum temperature of 5.7 °C and an average temperature of 3.6 °C, and a decrease inside the mouth, with a maximum temperature of 5.5 °C and an average temperature of 2.9 °C (Figure 6). This result is directly related to the route and intensity of the cold wave. The weather station data indicate that the cold water mass generated by the cold wave does not flow directly south but instead moves southeast

of the sea under the influence of the wind and waves, causing rapid cooling outside the mouth. Notably, the North Branch responds much more rapidly and obviously to the cold wave, with a maximum cooling of over $3.2\text{ }^{\circ}\text{C}$. In contrast, the South Branch, North Passage, and South Passage waters do not respond as quickly; however, their cooling is nearly universal during the same cold wave; for instance, during the cold wave in January 2015, they all cool by approximately $2\text{ }^{\circ}\text{C}$ (Figure 7a), and in December 2021, they all cool by approximately $1\text{ }^{\circ}\text{C}$ (Figure 7b). This decrease in SST inside the mouth and the mouth gate can be attributed to the diffusion of cold air from the south as a result of the cold wave driving a colder water mass, intensifying wind and wave action. These factors affect lower-latitude waters, resulting in lower temperatures within the Yangtze Estuary and at its mouth opening. Consequently, the response of the Yangtze Estuary waters to a cold wave, including the effect of dynamic wind deflection and thermal heat transfer, where the tides, currents, and SST exhibit both a conventional response and a response driven by the weather conditions of the cold wave, is a more complex process. However, the overall result is a significant short-term deviation from the Yangtze Estuary's SST.

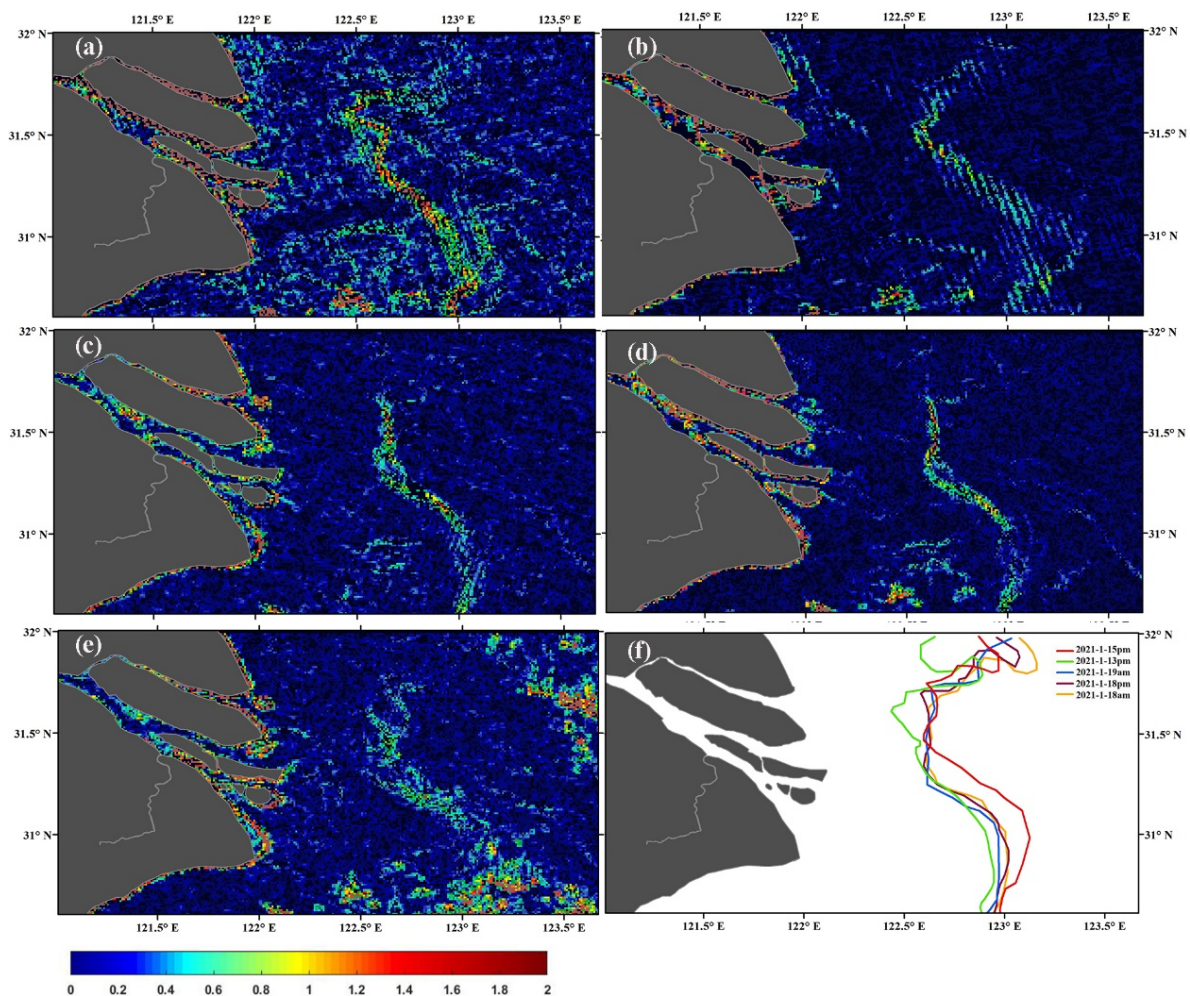


Figure 4. Frontal intensity ($^{\circ}\text{C}/\text{km}$) and spatial variation of temperature fronts in the Yangtze Estuary during the cold wave, where (a–e) represent the frontal intensity and its spatial distribution on the afternoon of 13 January (two days before the cold wave), the afternoon of 15 January (the day of the cold wave), the morning of 18 January (the day after the cold wave), the afternoon of 18 January (one day after the cold wave), and the intensity of temperature fronts and their spatial distribution in the afternoon of 19 January (2 days after the cold wave), and (f) is a brief description of the sea surface temperature front pattern based on the actual situation of the fronts obtained from the ArcGIS platform via digital image inversion.

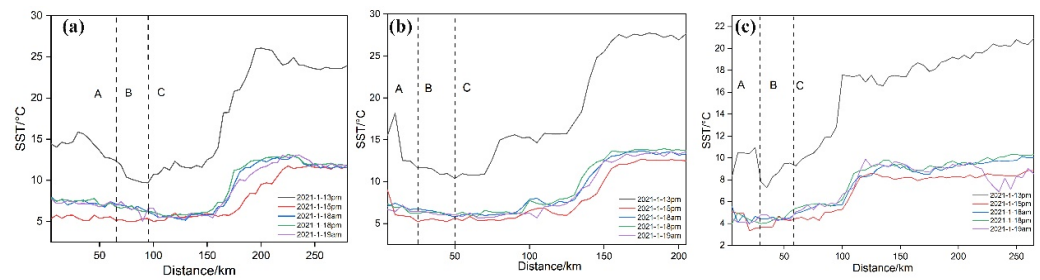


Figure 5. The effect of the cold wave on the SST field from inside the mouth to outside the mouth (using the January 2015 cold wave as an example), where A, B, and C represent inside the mouth, the mouth opening, and outside the mouth, respectively. (a–c) represent the three profiles P1, P2, and P3, respectively.

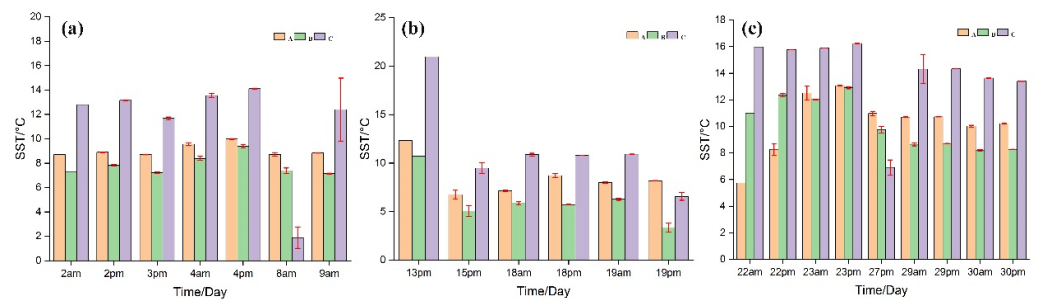


Figure 6. Changes in the SST of the Yangtze Estuary during the cold wave (where (a–c) represent the cold wave in January 2015, the cold wave in January 2021, and the cold wave in December 2021, the horizontal coordinates represent the date, am is morning, pm is afternoon, and the length of the red error bars represent the magnitude of the temperature change).

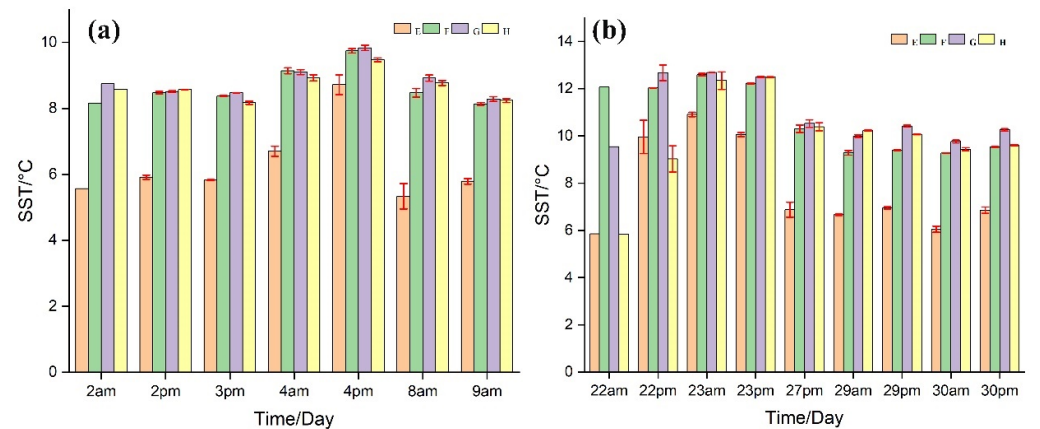


Figure 7. The effect of the cold wave process on the SST in the Yangtze Estuary (where (a,b) correspond to the cold waves in January 2015 and December 2021, respectively; E, F, G, and H correspond to the North Branch, South Branch, North Passage, and South Passage waters of the mouth of the Yangtze River, respectively; and the length of the red error bars represent the magnitude of the temperature change).

Cold waves alter the pattern of low–high temperature values in the Yangtze Estuary, as shown by the results of the profile analysis along with the SST from inside the mouth to outside the mouth (Figure 5). The SST is at its lowest inside the mouth, at the mouth opening, and outside the mouth. There is also a significant expansion in low temperatures outside the mouth. Furthermore, the temperature gradient between inside the mouth and the mouth opening is only 0.03 °C/km, while the temperature gradient from the

mouth opening to outside the mouth is $0.17\text{ }^{\circ}\text{C}/\text{km}$, which indicates a spatial pattern of low–lower–higher temperature.

As shown in Figures 4 and 8, the results of remote sensing inversion and the inversion of temperature fronts using a mathematical morphology edge detection algorithm demonstrate that cold waves alter the temperature field characteristics, as well as the intensity, morphology, and spatial distribution pattern of temperature fronts in the Yangtze Estuary. The boundary of the arc temperature front expands toward the outer sea and becomes further defined, exhibiting an uneven temperature distribution along the front. In the North Passage, North Trough, and South Trough, temperature shear fronts can be observed due to relatively large temperature differences in the trough and shallow turning areas. The main reason for this is the combined effect of cold winds, waves, and tides, which leads to flow shear and tidal phase differences between the Yangtze Estuary beaches. During the same period, strong coastal currents and sustained northerly winds forced the warm water masses from the outer sea to retreat to the southeast and shrink to south of $31^{\circ}30'\text{ N}$. A strong temperature front develops in the steeply sloping area between the southward coastal current, and the northward warm current gradually moves eastward from $122^{\circ}30'\text{ E}$ to 123° E with a temperature gradient of $0.5\text{--}1.2\text{ }^{\circ}\text{C}/\text{km}$ (Figure 4b,f). With the combined effects of strong tidal forces, warm currents with increased outward heat transfer intensity, and strong cold water masses resulting from gales and cold air waves, the interfacial temperature exhibits an irregular edge pattern that is more scattered.

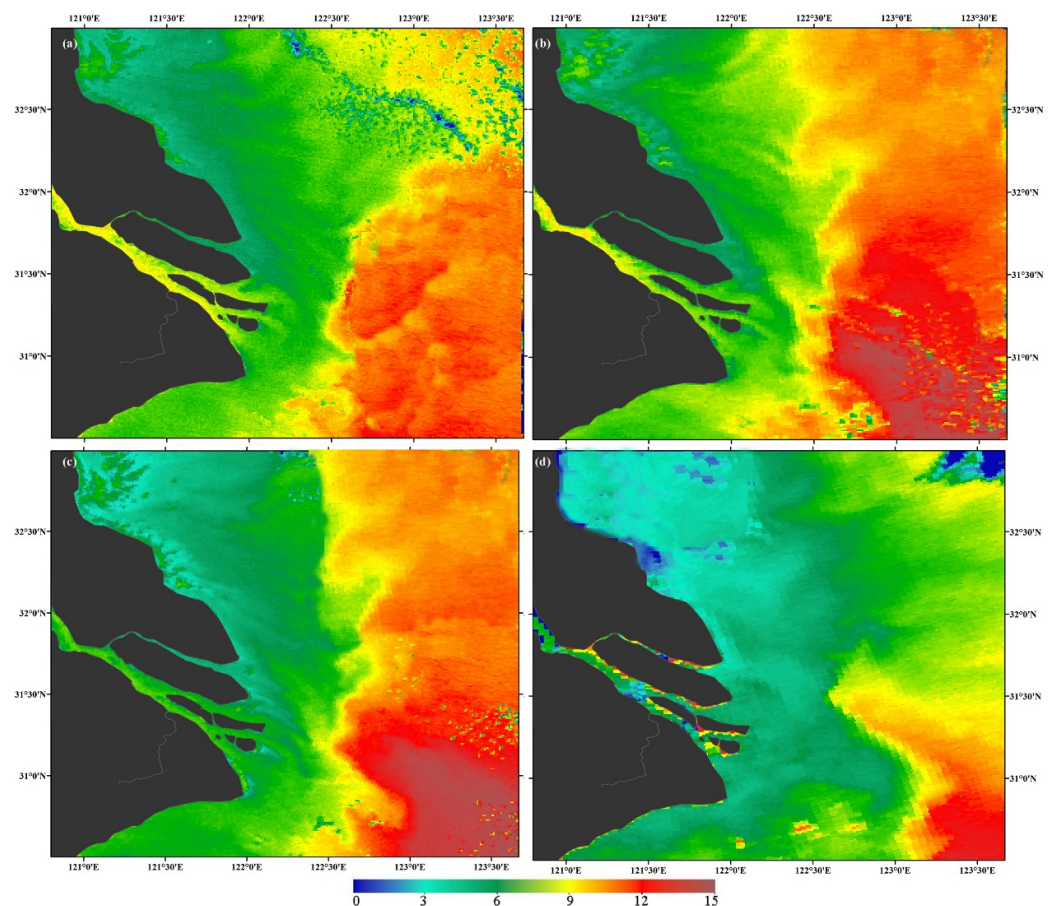


Figure 8. Characteristics of the temperature field in the Yangtze Estuary during the cold wave (where (a–d) represent the cold wave day data on 8 January 2015, 27 December 2021, 10 January 2018, and 15 January 2021, respectively).

3.4. Characteristics of the Yangtze Estuary's Temperature Field after a Cold Wave

The cold water masses propelled forward by a cold wave naturally retreat or completely evaporate after the cold wave passes. However, the SST in the Yangtze Estuary still exhibits low-temperature characteristics (Figure 9), with a local tendency to increase. However, the SST outside the mouth rises more rapidly, with an average rise of 5–9 °C, and the tongue border of the extreme temperature, pointing toward the Yangtze Estuary, becomes increasingly apparent. In addition, the temperature front generated by the convergence of the temperature tongue and the amount of cold water being transported by the Yangtze River runoff becomes increasingly evident. Even though the cold water masses are receding and the effects of the cold wave are still evident at the mouth opening, the average warming is only 1 to 2 °C (Figure 6). Inside the mouth, the average temperature increases by only 0.18–1 °C. The North Branch is warming more rapidly than the South Branch, the North Passage, the South Passage, or other marine regions (Figure 5). The land source and the cold water delivered by the Yangtze River flow downstream in winter have a greater impact on the SST inside the mouth. Even when other conditions, such as wind, waves, and tides, are considered, the temperature is lower than that during a cold wave. From inside the mouth to outside the mouth, the SST reverts to a low–high temperature trend. The average temperature gradient from inside the mouth to the mouth opening is 0.05 °C/km, which is a moderate shift in SST. However, with an average temperature gradient of 0.19 °C/km, the fluctuations in SST from the mouth opening to outside the mouth are much greater (Figure 5).

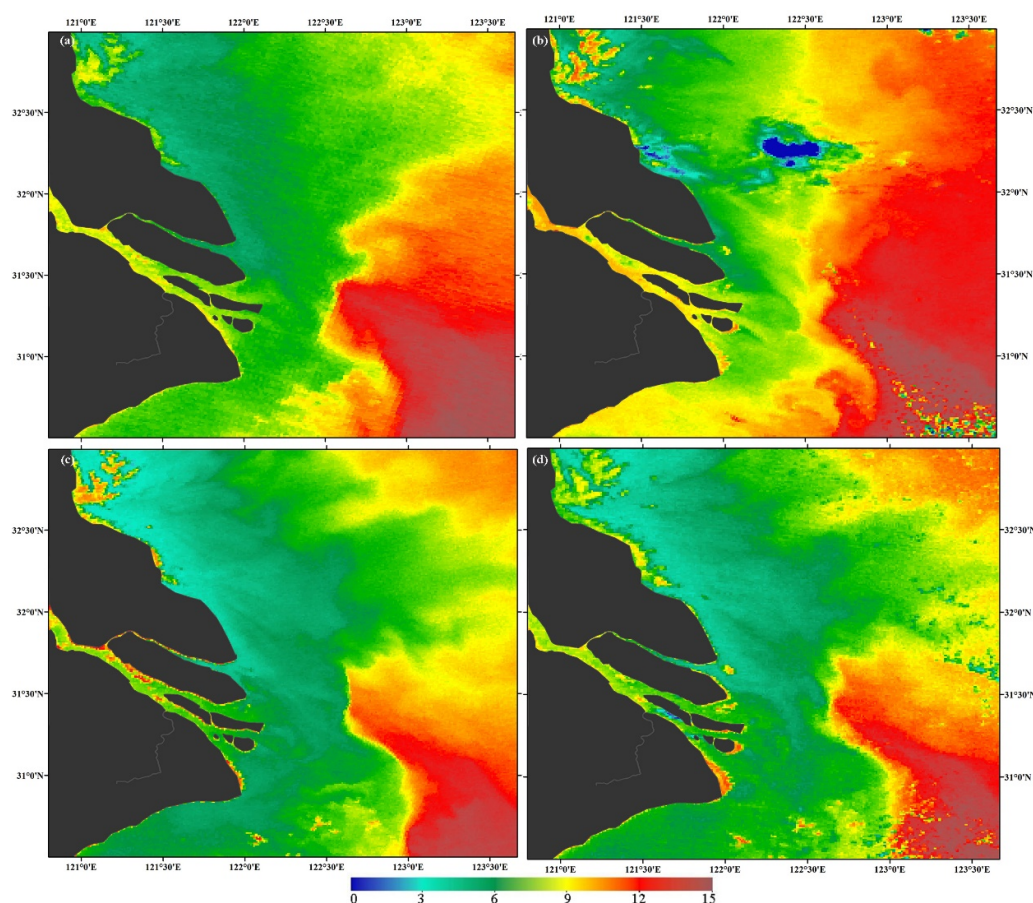


Figure 9. Characteristics of the temperature field in the Yangtze Estuary after the cold wave (where (a–d) are for 9 January 2015 (1 day after the cold wave), 30 December 2021 (2 days after the cold wave), and 18 January (1 day after the cold wave) and 19 January, 2021 (2 days after the cold wave), respectively).

Currently, there is no clear indication of the location of the arc temperature front. Shear temperature fronts are absent in the waters of the northern harbor, northern trough, and southern trough. As a result of runoff downstream, a large mass of cold water is deposited inside the mouth and near the shoreline, lowering the water temperature. The tongue-shaped mass of water outside the mouth has a higher temperature. Together, they form a temperature front with a gradient of 0.6~1.5 °C/km. Overall, the front moves slowly northwestward, with no significant changes occurring in the 31°20'–32° N section, whereas it moves slowly westward south of 31°20' N. The convex tongue continues to migrate southward, reaching a position near 31°~31°30' N (Figure 8c–f). Temperature fronts are influenced by tides. In small tides, the fronts are tongue-shaped and have a more regular shape with a more distinct frontal interface (Figure 9c,d), whereas at high tide, the frontal interface is affected by extremely strong tides, making it difficult to detect. Note that the influence of northerly winds has not yet completely receded and that the frontal interface still exhibits irregular edges (Figure 9a,b).

4. Conclusions

Bright temperature, sea surface emissivity, and atmospheric transmittance were calculated considering local factors to provide an optimum split-window algorithm with accuracy superior to that of MODIS SST products. MODIS data can be utilized to invert and analyze the temperature field of the Yangtze Estuary during a short period of typical cold weather. The MODIS inversion results of the SST of the Yangtze Estuary during a typical cold wave were used as base data, coupled with the temperature profile analysis method and the edge detection algorithm based on mathematical morphology to analyze and explore the changes in the SST characteristics of the Yangtze Estuary during a cold wave. Several points can be summarized.

- (1) The cold wave alters the temperature field characteristics and the intensity, morphology, and spatial distribution pattern of temperature fronts in the Yangtze Estuary for a short time. Cold water masses along the coast of the north spread out in a tongue-shaped pattern toward the southeast, and a nearshore current interacts with the masses and forms an east–west arc-shaped temperature front in the sea to the east of Chongming Island Beach. The cold wave also interacts with the tongue-shaped warm water masses outside the mouth, which can reach 31°30'~32° N, forming a strong temperature front near 122°E. While the arc-shaped temperature front extends into the outer sea during the cold wave, the boundary becomes more distinct; shear temperature fronts can also be seen in the northern harbor, northern trough, and southern trough waters. Additionally, the strong temperature front moves east to 122°30'~123° E, and the warm water mass begins to retreat south of 31°30' N. The strong temperature front exhibits irregular edge patterns and scattered patterns as a result of the combined effect of the cold water masses caused by the cold wave and tide, as well as the warm water currents outside the mouth. As cold waves retreat, the cold water mass generated by the cold wave recedes rapidly, continuously, or even vanishes, but the Yangtze estuarine waters maintain their low-temperature characteristics. The boundary of the arc-shaped temperature front becomes increasingly difficult to distinguish. Shear temperature fronts are not observed in the waters of the northern harbor, northern trough, and southern trough. The strong temperature front gradually moves northwest.
- (2) The cold wave results in significant short-term deviations in the SST of the Yangtze Estuary. The temperature line decreases rapidly with time when a cold wave is present. The cooling outside the mouth reaches a maximum of 12.2 °C, but the cooling inside the mouth is less than 5.5 °C. Inside the mouth, the Northern Branch responds most significantly to the cold wave, with a cooling amplitude of 3.2 °C. After the cold wave, the outside of the mouth warms rapidly, with an average warming up to 5~9 °C, while the inside warms very slowly, averaging only 0.18~1 °C.

- (3) Cold waves alter the spatial distribution of low-to-high temperatures in the Yangtze Estuary's temperature field. Before the cold wave, there is an average temperature gradient of 0.1 °C/km from the inside mouth to the mouth gate and an average temperature gradient of 0.29 °C/km from the mouth gate to the outside mouth. The Yangtze Estuary's SST is at its lowest level during the cold wave. This results in a temperature gradient of only 0.03 °C/km from inside the mouth to the mouth opening and 0.17 °C/km from the mouth opening to outside the mouth, indicating a pattern of low–lower–higher temperatures. A temperature gradient of 0.19 °C/km is observed from the mouth opening to outside the mouth after the cold wave, while a gradient of 0.05 °C/km occurs inside the mouth and at the mouth opening, which indicates that the spatial pattern of low–high temperature was restored.
- (4) Cold waves can significantly influence the strength, morphology, and distribution of the temperature front. In preparation for a cold wave, the temperature gradient of the front is 0.9~1.8 °C/km, with the frontal interface located near 122° 30' E, and a tongue bulges to the west at 31°30'~32° N. During the cold wave, the temperature gradient is 0.5~1.2 °C/km, the frontal interface gradually moves to 123° E, and the tongue bulging to the west gradually moves to 31°30' N south. Notably, after the cold wave, the temperature gradient is approximately 0.6 °C/km; the frontal interface of 31°20'~32° N does not vary significantly, but the frontal interface south of 31°20' N gradually moves to the west, and the tongue bulges to the west and continues to move to 31°~31°30' N.

The analysis of the characteristics of the SST changes in the Yangtze Estuary under the influence of a cold wave can help further understand the change pattern of SST and have a deeper overall understanding of the role between the SST and other environmental factors. This is of practical value and guidance to the fisheries production and short-term forecasting of SST in the Yangtze Estuary. It has theoretical and practical significance for estuarine ecosystem characteristics and disaster prevention and mitigation, environmental protection, etc.

Author Contributions: Conceptualization, X.J. and R.C.; methodology, R.C.; software, R.C.; validation, R.C.; formal analysis, R.C. and X.J.; investigation, R.C.; resources, X.J. and R.C.; data curation, R.C.; writing—original draft preparation, R.C.; writing—review and editing, R.C., X.J. and J.C. All authors have read and agreed to the published version of the manuscript.

Funding: This study was jointly supported by the Natural Science Foundation of China (No. 41376098) and National Key R & D Program of China, NO. 2017YFC0405503. Thanks would be extended to the anonymous reviewers for their invaluable and constructive suggestions, which greatly improved the quality of the paper.

Institutional Review Board Statement: Not applicable for studies not involving humans or animals.

Informed Consent Statement: Not applicable.

Data Availability Statement: Data is contained within the article.

Conflicts of Interest: No potential conflict of interest was reported by the authors.

References

1. Guan, L.; Chen, R.; He, M. Validation of sea surface temperature from ERS-1 /ATSR in the Tropical and Northwest Pacific. *J. Remote Sens.* **2002**, *6*, 63–69.
2. Cai, R.; Chen, J.; Huang, R. The response of marine environment in the offshore area of China and its adjacent ocean to recent global climate change. *Chin. J. Atmos. Sci.* **2006**, *30*, 15.
3. Wang, D.; Feng, X.; Zhou, L.; Hao, J.; Xu, X. Relationship between blue algal bloom and water temperature in Lake Taihu based on MODIS. *J. Lake Sci.* **2008**, *20*, 173–178.
4. Wang, J.; Wang, J.; Xu, J.; Luan, K.; Yang, Y.; Lv, Y. Characteristics of the Sea Surface Temperature Variation in Adjacent Area of the Yangtze River Estuary. *Adv. Mar. Sci.* **2020**, *38*, 624–634.
5. Sun, Q.; Xue, C.J.; Liu, J.Y.; Xue, C.J.; Liu, J.Y. Spatiotemporal association patterns between marine net primary production and environmental parameters in a view of data mining. *Mar. Environ. Sci.* **2020**, *39*, 340–347+352. [[CrossRef](#)]

6. Zhang, C.; Zhou, S.; Zhu, L. Three Algorithms of Sea Surface Temperature Inversion of Daya Bay Based on Environmental Satellite HJ-1B Data. *J. East China Inst. Technol.* **2013**, *36*, 88–92.
7. Hu, H. Impact of the Reservoirs on Downstream Water Temperature Variation Research Based on River Temperature Remote Sensing. Master's Thesis, Huazhong University of Science & Technology, Wuhan, China, 2018.
8. Mai, J.; Jiang, X. Analysis of sea surface temperature variations in the Yangtze Estuarine waters since 2000 using MODIS. *J. Remote Sens.* **2015**, *19*, 818–826.
9. Hu, H.; Hu, F. Water types and frontal surface in the Changjiang Estuary. *J. Fish. Sci. China* **1995**, *2*, 10.
10. Chen, J.; Jiang, D.; Zhang, X. Reconstruction of temporal and spatial distribution characteristics of sea surface temperature in the Yangtze River Estuary based on dynamic mode decomposition method. *J. Zhejiang Univ. Sci. Ed.* **2022**, *49*, 76–84.
11. Chen, M.; Shi, S.; Shen, H. Relationship between surface seawater temperature in the Yangtze estuary and El Niño event. *Mar. Forecast.* **2005**, *1*, 80–85.
12. Jiménez-Muñoz, J.C.; Sobrino, J.A. A generalized single-channel method for retrieving land surface temperature from remote sensing data. *J. Geophys. Res. Atmos.* **2003**, *108*, D22. [[CrossRef](#)]
13. Sobrino, J.A.; Jimenez-Munoz, J.C.; Paolini, L. Land surface temperature retrieval from LANDSAT TM 5. *Remote Sens. Environ. Interdiscip. J.* **2004**, *90*, 434–440. [[CrossRef](#)]
14. Huang, M.; Mao, Z.; Xing, X.; Sun, Z.; Zhao, Z.; Huang, W. A Model for Water Surface Temperature Retrieval from HJ-1B/IRS Data and Its Application. *Remote Sens. Land Resour.* **2011**, *6*, 81–86.
15. Zhou, X.; Yang, X.; Lv, X.; Li, Z.; Tao, Z. The retrieval of the single-channel sea surface temperature using infrared radiative transfer model. *J. Trop. Meteorol.* **2012**, *28*, 6.
16. Tan, Z.; Minghua, Z.; Karnieli, A.; Berliner, P. Mono-window Algorithm for Retrieving Land Surface Temperature from Landsat TM6 data. *Acta Geogr. Sin.* **2001**, *56*, 456–466.
17. McMillin, L.M. Estimation of sea surface temperatures from two infrared window measurements with different absorption. *J. Geophys. Res.* **1975**, *80*, 5113–5117. [[CrossRef](#)]
18. Liu, L.; Zhou, J. Using MODIS Imagery to Map Sea Surface Temperature. *Geospat. Inf.* **2006**, *2*, 7–9.
19. Zhang, C.; Zhang, X.; Zeng, Y.; Pan, W.; Lin, J. Retrieval and validation of sea surface temperature in the Taiwan Strait using MODIS data. *Acta Oceanol. Sin.* **2008**, *30*, 153–160.
20. Zhu, L.; Gu, X.; Wang, Q.; Yu, T.; Li, L. A Regional Algorithm to Estimate Sea Surface Temperature in the East China Sea. *Remote Sens. Technol. Appl.* **2008**, *5*, 495–499.
21. Hu, T.; Shen, S.; Shi, C.; Wu, Y.; Wu, Z. Retrieval and Evaluation of 20-year Sea Surface Temperature Sequence Data Sets. *Meteorol. Sci. Technol.* **2012**, *40*, 571–577. [[CrossRef](#)]
22. Wan, Z.; Dozier, J. A generalized split-window algorithm for retrieving land-surface temperature from space. *IEEE Trans. Geosci. Remote Sens.* **1996**, *34*, 892–905.
23. Mao, K.; Qin, Z.; Shi, J.; Gong, P. A practical split-window algorithm for retrieving land-surface temperature from MODIS data. *Int. J. Remote Sens.* **2005**, *26*, 3181–3204. [[CrossRef](#)]
24. Qin, Z.; Karnieli, A.; Berliner, P. A mono-window algorithm for retrieving land surface temperature from Landsat TM data and its application to the Israel-Egypt border region. *Int. J. Remote Sens.* **2010**, *22*, 3719–3746. [[CrossRef](#)]
25. Gao, M.; Tan, Z.; Gao, M.; Zhang, C.; Sebu, L. Calibration of View Angle for Retrieving Land Surface Temperature from the Moderate Resolution Imaging Spectroradiometer (MODIS). *Remote Sens. Technol. Appl.* **2007**, *36*, 433–437.
26. Ri, C.; Liu, Q.; Li, H.; Fang, L.; Sun, D. Improved split window algorithm to retrieve LST from Terra/MODIS data. *J. Remote Sens.* **2013**, *17*, 830–840.
27. Xie, Y.; Ke, L.; Wang, D. Screening of microorganism agents for liriodendron chinense tissue culture seeding and preliminary study on its mechanism. *Chin. J. Biol. Control* **2018**, *20*, 281–288.
28. Hou, J.; He, J.; Jin, X.; Hu, T.; Zhang, Y. Study on optimisation of extraction process of tanshinone II A and its mechanism of induction of gastric cancer SGC7901 cell apoptosis. *Afr. J. Tradit. Complement. Altern. Med. Ajtcam* **2018**, *10*, 456–458. [[CrossRef](#)]
29. Oates, C.J.; Girolami, M.; Chopin, N. Control functionals for more carlo integration. *J. R. Stat. Soc.* **2018**, *79*, 695–718. [[CrossRef](#)]
30. Fortino, G.; Russo, W.; Savaglio, C.; Shen, W. Agent-oriented cooperative smart objects: From IoT system design to implementation. *IEEE Trans. Syst. Man Cybern. Syst.* **2018**, *48*, 1939–1956. [[CrossRef](#)]
31. Yin, L.; Kang, Y.J.; Lee, K. Study on the development of smart jewelry in the IoT environment. *IEEE Trans. Syst. Man Cybern. Syst.* **2018**, *9*, 19. [[CrossRef](#)]
32. Meneghesso, C.; Seabra, R.; Broitman, B.R. Remotely-sensed L4 SST underestimates the thermal fingerprint of coastal up-welling. *Remote Sens. Environ.* **2019**, *237*, 111588–111598. [[CrossRef](#)]
33. Merchant, C.J.; Embury, O.; Bulgin, C.E. Satellite-based time-series of sea-surface temperature since 1981 for climate applications. *Sci. Data* **2019**, *6*, 223–241. [[CrossRef](#)] [[PubMed](#)]
34. Bai, M.; Wu, H. Characteristics of sea surface temperature in the Changjiang Estuary and adjacent waters based on a Self-Organizing Map. *J. East China Norm. Univ. (Nat. Sci.)* **2018**, *2018*, 184–194.
35. Huang, B.; Deng, R. Pervasive single-channel algorithm-based Yangtze River mouth temperature inversion using HJ-1B data. *Anhui Agric. Sci. Bull.* **2019**, *25*, 145–146. [[CrossRef](#)]
36. Ghasemi, A.R. Influence of northwest Indian Ocean sea surface temperature and El Niño–Southern Oscillation on the winter precipitation in Iran. *J. Water Clim. Chang.* **2020**, *11*, 1481–1494. [[CrossRef](#)]

37. Ma, W.; Peng, H.; Wu, L.; Meng, H. Interannual variation patterns of sea surface temperature anomaly in the Southern Ocean. *Period. Ocean Univ. China* **2022**, *52*, 26–33. [[CrossRef](#)]
38. Brady, F.; Bulusu, S.; Alison, M. Confirmation of ENSO-Southern Ocean Teleconnections Using Satellite-Derived SST. *Remote Sens.* **2018**, *10*, 331.
39. Xu, X.; Dai, J.; Yin, H. The Characteristics of Cold Wave in Shanghai during Recent 20 Years. *Atmos. Sci. Res. Appl.* **2009**, *1*, 73–80.
40. Esaias, W.E.; Abbott, M.R.; Barton, I.; Brown, O.B.; Minnett, P.J. An overview of MODIS capabilities for ocean science observations. *IEEE Trans. Geosci. Remote Sens.* **1998**, *36*, 1250–1265. [[CrossRef](#)]
41. Donlon, C.J.; Minnet, P.J.; Gentemann, C.; Nightingale, T.J.; Barton, I.J. Toward Improved Validation of Satellite Sea Surface Skin Temperature Measurements for Climate Research. *J. Clim.* **2002**, *14*, 353–369. [[CrossRef](#)]
42. Qin, Z.; Dall’Olmo, G.; Karnieli, A. Derivation of split window algorithm and its sensitivity analysis for retrieving land surface temperature from NOAA-advanced very high resolution radiometer data. *J. Geophys. Res. Atmos.* **2001**, *10*, 22655–22670. [[CrossRef](#)]
43. Zhao, Y. *Principles and Methods of Remote Sensing Application Analysis*; Science Press: Beijing, China, 2003.
44. Ottle, C.; Stoll, M. Effect of atmospheric absorption and surface emissivity on the determination of land surface temperature from infrared satellite data. *Int. J. Remote Sens.* **1993**, *14*, 2025–2037. [[CrossRef](#)]
45. Liang, S.; Li, X.; Wang, J. *Quantitative Remote Sensing: Concepts and Algorithms*; Science Press: Beijing, China, 2013.
46. Niclòs, R.; Valor, E.; Caselles, V.; Coll, C.; Sánchez, J. In situ angular measurements of thermal infrared sea surface emissivity—Validation of models. *Remote Sens. Environ.* **2005**, *94*, 83–93. [[CrossRef](#)]
47. Hulley, G.C.; Hook, S.J.; Schneider, P. Optimized split-window coefficients for deriving surface temperatures from inland water bodies. *Remote Sens. Environ.* **2011**, *115*, 3758–3769. [[CrossRef](#)]
48. Kaufman, Y.J.; Gao, B.C. Remote sensing of water vapor in the near IR from EOS/MODIS. *IEEE Trans Geosci. Remote Sens.* **1992**, *30*, 871–884. [[CrossRef](#)]
49. Mai, J. Remote Sensed Analysis on Sea Surface Temperature Variations in the Yangtze Estuarine Waters since Year 2000. Master’s Thesis, East China Normal University, Shanghai, China, 2015.
50. Gao, M.F.; Qin, Z.H.; Xu, B. Estimation of the basic parameters for deriving surface temperature from MODIS data. *Arid Zone Res.* **2007**, *24*, 7.
51. Minnett, P.J.; Brown, O.B.; Evans, R.H.; Key, E.L.; Kearns, E.J.; Kilpatrick, K.; Kumar, A.; Maillet, K.A.; Szczodrak, G. Sea-surface temperature measurements from the Moderate-Resolution Imaging Spectroradiometer (MODIS) on Aqua and Terra. In Proceedings of the IEEE International Geoscience & Remote Sensing Symposium, Anchorage, AK, USA, 20–24 September 2004.
52. Shimada, T.; Sakaida, F.; Kawamura, H.; Okumura, T. Application of an edge detection method to satellite images for distinguishing sea surface temperature fronts near the Japanese coast. *Remote Sens. Environ.* **2005**, *98*, 21–34. [[CrossRef](#)]
53. Lian, J.; Wang, K. An Image Edge Detection Method Based on Multi-scale Morphology. *Comput. Eng. Appl.* **2006**, *42*, 3.

Disclaimer/Publisher’s Note: The statements, opinions and data contained in all publications are solely those of the individual author(s) and contributor(s) and not of MDPI and/or the editor(s). MDPI and/or the editor(s) disclaim responsibility for any injury to people or property resulting from any ideas, methods, instructions or products referred to in the content.